Predictions of the transient loading on box-like objects by arbitrary pressure waves in air

H.L. Gauch[a], V. Bisio[b], S. Rossin[b], F. Montomoli[a], V.L. Tagarielli[a,*]

[a]*Department of Aeronautics, Imperial College London, SW7 2AZ, UK*
[b]*Baker Hughes, a GE company, Via Felice Matteucci 2, 50127 Firenze FI, Italy*

Abstract

This study investigates the transient loading on rigid, isolated, box-like objects by impinging pressure waves of variable intensity and time duration. A numerical solver is used to predict the transient flow around the object and the consequent pressure on the object's surface. An analytical model is developed which is capable of predicting the transient loading history on the faces of a box-like object; it was found in good agreement with the numerical predictions. The numerical and analytical models are then used to construct non-dimensional design maps. Different regimes of loading are identified and explored.

Keywords: drag, transient flow, pressure wave, shock wave, diffraction, clearing

1. Introduction

Numerous studies have been published on the transient loading of objects by shock waves, due to the relevance of the problem to the defence industry and to safety in general. Compared to loads resulting from steady state flow of similar particle velocity, the loads exerted on a body by a shock wave can be up to one order of magnitude greater in amplitude [1, 2]. These loads can be predicted for some simple geometries (e.g. for the case of a flat surface [3, 4]). Much less research has focused on the case of pressure waves with finite rise time and longer durations. This type of loading can be encountered in different applications, for example as a consequence of deflagration, which is a threat to safety of operations in several industries (e.g. chemical and oil&gas) [5, 6, 7].

The reflection of a shock wave from an infinitely large, planar, rigid surface gives rise to an at least twofold increase in overpressure on the surface, which can be calculated using reflection coefficients obtained from simple gas dynamics (e.g. [8]). However, if the surface is

of finite size, rarefaction waves are generated at its edges and travel inwards, alleviating the pressure over time. This effect was estimated in a simple manner in [3], assuming a linear decrease in pressure from reflected pressure to stagnation pressure. A more detailed modelling approach was developed by Hudson [4]. This approach employs sound pulse theory [9, 10] to estimate the strength of the rarefaction waves spreading from the surface's edges. These rarefaction waves are then superimposed to the reflected wave to obtain a transient load on the front surface; the model was found in good agreement with experiments [11, 12]. A similar approach was presented by Merritt [13] for the case of pressure waves of finite rise time and short duration.

Most studies on shock waves model the reflection and diffraction of the waves at an obstacle. However, in the case of waves of sufficiently long rise time and duration, it is expected that the inertial flow around the object will have a significant influence on the loading history. Research into the physics of accelerated flow past objects and on multi-phase flow has touched on this question from a more fundamental perspective. Magnaudet and Eames [14] suggested that the force on a particle immersed in an unsteady flow can be categorised into five contributions, namely quasi-steady, inviscid unsteady, viscous unsteady, lift, and buoyancy-gravity, i.e.

$$\boldsymbol{F}(t) = \boldsymbol{F}_{\mathrm{qs}}(t) + \boldsymbol{F}_{\mathrm{iu}}(t) + \boldsymbol{F}_{\mathrm{vu}}(t) + \boldsymbol{F}_{\mathrm{l}}(t) + \boldsymbol{F}_{\mathrm{bg}}(t). \tag{1}$$

*Corresponding author, Email: v.tagarielli@imperial.ac.uk

Early published work on the loading of rectangular objects [3, 4, 13] neglects all of these contributions except for wave reflection and diffraction, which fall into the inviscid unsteady group [15]. Numerous authors [16, 17, 18, 19, 20] have shown that flow acceleration causes another force contribution which is known as added-mass force in the incompressible flow regime [21].

In this paper we develop a predictive model for the transient loads experienced by a box-like object due to the impact of an arbitrary pressure wave. First, we perform detailed two-dimensional computational fluid dynamics (CFD) calculations to predict the transient flow due to arbitrary pressure waves impinging on a rectangular object. Then, an analytical model is constructed and validated against the CFD predictions. Both models are then used to explore the different regimes of behaviour in this problem and to construct non-dimensional design maps of immediate application. In concurrent work, the authors have conducted a similar analysis for the case of a circular cylinder [22].

2. Problem definition

A planar pressure wave of length λ_i, rise coefficient α_r and maximum overpressure p_i impinges on a rigid, rectangular object of height H and depth W, which is clamped to the ground as in Fig. 1. The initial overpressure distribution along the wave is assumed to be triangular. The surrounding medium, air, is characterised by the heat capacity ratio $\gamma = 1.4$, the specific gas constant $R = 287\,\mathrm{J\,kg^{-1}\,K^{-1}}$ and a reference static pressure and temperature p_0 and T_0, respectively. The aim of this study is to find the transient pressure loads on the surfaces of the rectangle.

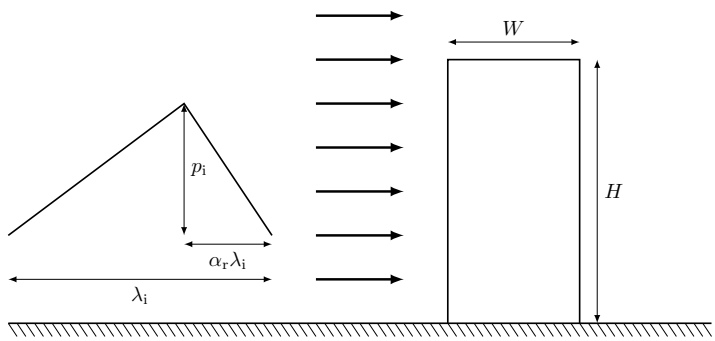

Figure 1: Pressure wave of variable shape impinging on a rectangular structure.

As the tail of the incoming wave travels at the ambient speed of sound, c_0, the wave duration can be expressed as

$$t_\mathrm{i} = \frac{\lambda_\mathrm{i}}{c_0}, \qquad c_0 = \sqrt{\gamma R T_0}. \tag{2}$$

Dimensional analysis of the problem suggests the non-dimensional sets

$$\begin{aligned} \bar{W} &= \frac{W}{H}, \qquad \bar{p}_\mathrm{i} = \frac{p_\mathrm{i}}{p_0}, \quad \tau_\mathrm{i} = \frac{t_\mathrm{i}}{H/c_0} = \frac{\lambda_\mathrm{i}}{H}, \quad \alpha_\mathrm{r}, \\ Re_\mathrm{i} &= \frac{\rho_\mathrm{i} v_\mathrm{i} H}{\mu_\mathrm{i}}, \quad \gamma, \qquad\qquad \tau = \frac{t}{H/c_0}, \end{aligned} \tag{3}$$

where ρ_i, v_i and μ_i denote the maximum density, particle velocity and dynamic viscosity of the fluid within the incident wave, respectively. Functional relationships between ρ_i, v_i and the pressure wave coefficients p_i, α_r, τ_i are given in Appendix A.

3. Models and methods

We proceed to present the numerical and analytical modelling approaches and to compare their predictions.

3.1. Numerical model

The surrounding gas is modelled as a perfect gas with heat capacity ratio $\gamma = 1.4$, so that the compressible, unsteady Navier-Stokes equations govern the behaviour of the flow. These were solved in their Reynolds-averaged form (URANS) using the rhoCentralFoam solver [23], which is part of the open-source CFD software package OpenFOAM [24], version 2.3.1. The viscosity of the gas was assigned a temperature-independent value, which was varied from case to case to achieve flow situations of different Reynolds numbers, whilst keeping the height H of the object at a constant value for all simulations to facilitate mesh generation. The assumption of temperature-independent viscosity was found to be appropriate due to the negligible influence of the Reynolds number above a certain value, as it will be detailed later in this section. The k-ω -SST model [25] was used as turbulence closure in all simulations.

The boundary conditions were of symmetry type for the top and bottom of the rectangular domains modelled. Zero-gradient boundary conditions were assigned at the left and right end of the domains; a no-slip condition was enforced on the velocity field on the edges of the object. Wall functions were used on this boundary for the variables of the turbulence model, for the sake of computational efficiency. Unwanted wave reflections from the boundaries of the analysed domains were precluded by choosing a sufficiently large domain size. To decrease the computational effort, a two-dimensional flow was analysed, necessitating only one cell over the thickness of the domain. While the assumption of two-dimensionality is accurate for the initial wave diffraction [1], resolving in detail the flow structures in the wake of the object would necessitate a three-dimensional approach. However, other researchers have found reasonable agreement, in terms of drag, comparing two-dimensional URANS simulations to experiments, 3D URANS and large eddy simulations for high-Reynolds-number flows past bluff bodies [26, 27, 28, 29].

The pressure wave or shock wave was modelled as an initial field of pressure, particle velocity and temperature. The equations defining the spatial distributions of these quantities as a function of the parameters p_i, α_r, τ_i are given in Appendix A. The rest of the fluid domain was assigned homogeneous initial conditions of $p = p_0$, $T = T_0$, $v = 0\,\mathrm{m\,s^{-1}}$. Figure 2a shows the computational domain and the initial pressure contours for the case $\alpha_\mathrm{r} = 0.5$, $\tau_\mathrm{i} = 30$, $\bar{p}_\mathrm{i} = 1$. This corresponds to an incoming pressure profile in the shape of an isosceles triangle, of overpressure equal to ambient pressure, impinging on a square shaped object of a side length corresponding to 1/30 of the incoming wave length. The front of the pressure wave is initially placed right in front of the object, such that the loading of the object begins at $t = 0$.

The used integration schemes were of first order in time and second order in space. Due to the explicit prediction of the fluxes in the rhoCentralFoam solver [23], the maximum time step was determined by enforcing the Courant-Friedrichs-Lewy (CFL) number to stay below 0.1. Interpolation of the convective terms was accomplished with the scheme by Kurganov and Tadmor [30], employing flux limiters after van Leer [31], as recommended in [23].

In order to efficiently simulate cases for a wide range of wave lengths, i.e. $\tau_\mathrm{i} \in [1, 100]$, the domain size and cell distribution need to be adapted to the individual cases. An unstructured grid consisting of quadratic cells of varying size was used for all computations. Due to the high local gradients of the flow, the cells were successively refined towards the object surface to a side length of $\Delta x_\mathrm{edges}/H = 0.0015$ at the edges and $\Delta x_\mathrm{corners}/H = 0.000375$ at the sharp corners of the rectangular body. The maximum cell size in the whole domain was limited to

$$\Delta x_\mathrm{max} = \frac{c_0 t_\mathrm{i}}{n_\mathrm{wave}}, \qquad n_\mathrm{wave} = 200. \tag{4}$$

In Fig. 2b an extract of the mesh for the case $\alpha_\mathrm{r} = 0.5,\ \tau_\mathrm{i} = 30,\ \bar{p}_\mathrm{i} = 1$ is depicted. The cells were successively refined towards the object surface to improve the resolution of the zones with the highest gradients due to wave diffraction, boundary layers, flow separation, and vortex shedding.

3.1.1. Mesh convergence study

An extensive mesh convergence study was conducted to estimate the spatial and temporal discretisation errors of the CFD simulations. Wide ranges of the non-dimensional parameters $\bar{p}_\mathrm{i}$, α_r, τ_i, $\bar{W}$, Re_i were explored in this study.

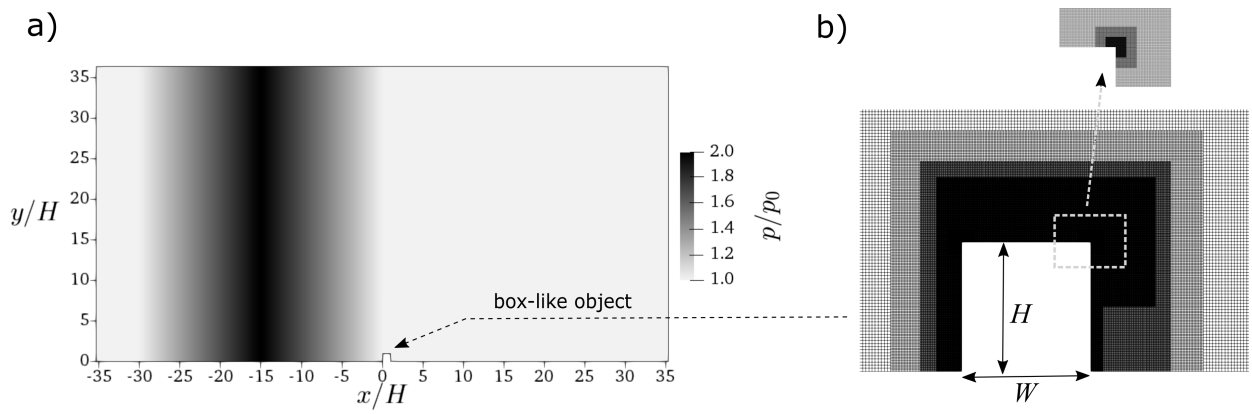

Figure 2: Assigned initial pressure field (a) and successively refined mesh around the box-like object (b) for the simulation of the case $\alpha_r = 0.5,\ \tau_i = 30,\ \bar{p}_i = 1$.

The following sets of discreet parameters were considered

$$\begin{aligned} &\alpha_r = \{0, 0.5\}, \qquad \bar{p}_i = \{0.1, 1, 3\}, \qquad \bar{W} = \left\{0.1\bar{W}_0, 3\bar{W}_0\right\}, \\ &\tau_i = \{1, 10, 100\}, \quad Re_i = \left\{10^2, 10^4, 10^6, 10^8\right\}, \end{aligned} \tag{5}$$

where the highest pressure ratio was omitted for the finite rise time case $\alpha_r = 0.5$, as pressure waves of this amplitude would turn into shock waves very rapidly. Spatial and temporal convergence were investigated for a total of 120 cases following the widely used methodology proposed by Roache [32]. We consistently use the grid convergence index (GCI) of the form [32]

$$\mathrm{GCI} = \frac{F_s}{(r_\Delta)^{\hat{p}} - 1}\left|\frac{f_2 - f_1}{f_1}\right|, \tag{6}$$

where F_s denotes a factor of safety, $\hat{p}$ the observed order of convergence, r_Δ the mesh refinement factor, and $f_1,\ f_2$ denote scalar solution values obtained on the finest and second finest grid. The observed order of convergence can be computed as

$$\hat{p} = \frac{\ln\left(\frac{f_3 - f_2}{f_2 - f_1}\right)}{\ln(r_\Delta)}. \tag{7}$$

Typically, values for $\hat{p}$ around one were obtained, which is to be expected, as the spatial discretisation scheme reduces to first order in the vicinity of shocks and mesh discontinuities (e.g. sharp corners) [33].

Three meshes were used for each case, with an isotropic refinement factor of $r_\Delta = 1.5$. Applying the recommendations proposed by Roy [34] for the factor of safety and the limits of $\hat{p}$, we obtained the maximum and mean GCI values across all investigated cases listed in Table 1. The chosen solution variables were the maximum average pressure across the front and back surface, $\bar{p}_{f,max}$ and $\bar{p}_{b,max}$, the maximum difference between these two, F_{max}, and the times at which these maxima were recorded, $t_{f,max},\ t_{b,max}$ and $t_{F,max}$. It can be seen that all found GCI values were well below 10%, except for the time to maximum back pressure. The back pressure can be subject to large oscillations in time due to vortex shedding and high speed flow around the sharp rear corner, which have proved to be somewhat grid sensitive in extreme cases.

Table 1: Maximum and mean values of the grid convergence index across all the simulations of the mesh convergence study

	$p_{f,max}$	$p_{b,max}$	F_{max}	$t_{f,max}$	$t_{b,max}$	$t_{F,max}$
$\mathrm{GCI}_{max}[\%]$	1.98	2.78	8.87	2.35	21.34	4.92
$\mathrm{GCI}_{mean}[\%]$	0.41	0.34	1.21	0.88	3.14	1.64

3.1.2. Influence of Reynolds number

Before defining the parameter set for the parametric CFD study, the influence of the Reynolds number is examined on the basis of the mesh convergence cases. In Table 2 we present the maximum relative differences in the solution variables $\bar{p}_{\mathrm{f,max}}$, $\bar{p}_{\mathrm{b,max}}$, F_{max} between the lower Reynolds numbers and $Re_{\mathrm{i}} = 10^8$, across all investigated cases. It can be seen that for $Re_{\mathrm{i}} \geq 10^4$ the relative differences in all solution variables fall below 5%. This apparent Reynolds number independence can be attributed to the sharp leading and trailing edges of the object, which represent distinct separation points of the flow. Consequently, the simulations presented in this study are conducted at a single Reynolds number, $Re_{\mathrm{i}} = 10^8$, representative of cases with $Re_{\mathrm{i}} \geq 10^4$, in good approximation.

Table 2: Maximum relative difference in the main solution variables between $Re_{\mathrm{i}} = 10^8$ and lower Reynolds numbers for the mesh convergence cases.

Re_{i}	$\left\lvert \frac{\bar{p}_{\mathrm{f,max},Re_{\mathrm{i}}} - \bar{p}_{\mathrm{f,max},10^8}}{\bar{p}_{\mathrm{f,max},Re_{\mathrm{i}}}} \right\rvert$ [%]	$\left\lvert \frac{\bar{p}_{\mathrm{b,max},Re_{\mathrm{i}}} - \bar{p}_{\mathrm{b,max},10^8}}{\bar{p}_{\mathrm{b,max},Re_{\mathrm{i}}}} \right\rvert$ [%]	$\left\lvert \frac{F_{\mathrm{max},Re_{\mathrm{i}}} - F_{\mathrm{max},10^8}}{F_{\mathrm{max},Re_{\mathrm{i}}}} \right\rvert$ [%]
10^2	6.96	15.3	9.58
10^4	1.08	2.61	3.51
10^6	0.18	1.31	0.80

3.1.3. Parametric study

An extensive parametric study was conducted. The space of the governing non-dimensional parameters was discretised as

$$\begin{aligned} \bar{W} &= \left\{0.1\bar{W}_0, 0.3\bar{W}_0, 1\bar{W}_0, 3\bar{W}_0\right\}, \qquad \bar{p}_{\mathrm{i}} = \{0.1, 0.5, 1, 1.5, 2, 3\}, \\ \tau_{\mathrm{i}} &= \{1, 5, 10, 20, 30, 50, 75, 100\}, \quad \alpha_{\mathrm{r}} = \{0, 0.25, 0.5\}, \end{aligned} \tag{8}$$

and most combinations of the parameters were explored (a total of 512 cases, for $Re_{\mathrm{i}} = 10^8$). Simulations were conducted in a high performance computing cluster, using 16 processors per case. Running times were between 1 hour and three days.

3.2. Analytical model

We pursue a simple analytical model able to capture the most important physical aspects of the problem, without the significant computational effort of the CFD model.

The outset of the new model is the force parametrisation after Magnaudet and Eames [14], given in Eq. (1). As in Parmar et. al [15], the viscous unsteady, lift, and buoyancy-gravity force contributions are neglected. The inviscid unsteady force, $\boldsymbol{F}_{\mathrm{iu}}$, consists of two parts, namely a pressure gradient and a history term. Parmar et al. [15] define the former to be due to pressure gradients in the flow which exist in absence of the object, and the latter to be due to the acceleration of the ambient fluid. We argue however that, in the present case, the pressure gradient force is more accurately described as force resulting from the reflection and diffraction of the incoming pressure wave. The force parametrisation therefore reads

$$\begin{aligned} \boldsymbol{F}(t) &= \boldsymbol{F}_{\mathrm{qs}}(t) + \boldsymbol{F}_{\mathrm{iu}}(t) \\ &= \boldsymbol{F}_{\mathrm{qs}}(t) + \boldsymbol{F}_{\mathrm{diff}}(t) + \boldsymbol{F}_{\mathrm{hist}}(t). \end{aligned} \tag{9}$$

We will proceed by introducing different models for each of the three terms in Eq. (9).

3.2.1. Propagation of a finite amplitude wave

The analytical models described in the following make use of time-dependent values of the flow variables pressure, particle velocity, density, temperature, and Mach number. As defined in Section 2, we assume an incoming wave of triangular pressure-space (and approximately pressure-time) evolution. At $t = 0$, the front of the wave has reached the front surface of the structure. Subsequently, the wave propagates past the object, generating a transient flow field. As

the pressure waves of interest in this study are of significant amplitude, $\bar{p}_\mathrm{i}$, the wave shape distorts during propagation due to the local differences in speed of sound and particle velocity (e.g. [35]). This effect is further enhanced by the wave diffraction and reflection, which increase the differences in the local properties across the wave.

A semi-analytical approach based on the method of characteristics is used to compute the time-dependent flow variables around the structure: The incoming wave is split into 100 individual 'wavelets' of different particle velocity and local speed of sound (see Appendix A). After a time step, the j-th wavelet has advanced by the distance, $\Delta x_j = (c_j + v_j)\Delta t$, leading to a distortion of the initial wave shape. The cases of a shock wave or a pressure wave developing into a shock wave need special treatment. In first approximation, a shock front propagates at the mean value of the velocities of the simple waves in front and behind the shock front [8]. The wavelets behind the shock front therefore propagate faster and, by catching up with the wave front, continuously change the pressure and velocity of the shock front.

The procedure is illustrated in Fig. 3, which shows the distortion of a finite amplitude wave, the transition to a shock wave once the wave front is overtaken by the wavelets behind it, and the decay of the maximum pressure after the peak of the wave has overtaken the front. At every point in space or time, the arrival of the individual wavelets determine the distributions of pressure, which are interpolated linearly to approximate the distorted wave shape. This simple procedure yields time-dependent flow properties of good accuracy at different positions (note that $x = 0$ at the front edge and $x = W$ at the back edge).

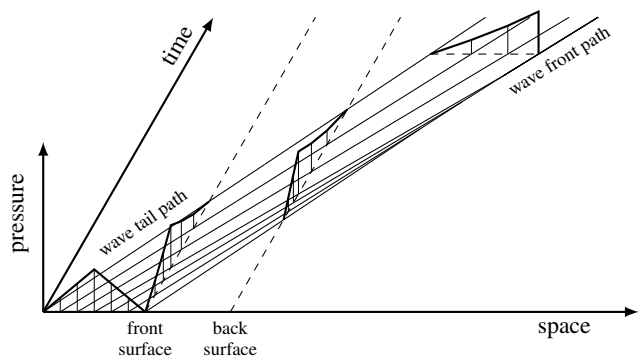

Figure 3: Prediction of the distortion of a finite amplitude wave with the method of characteristics. Superposed curves show the wave shape in terms of pressure for points in time and space.

3.2.2. Diffraction model

When a pressure wave encounters a rigid object, it is subject to reflection and diffraction, which cause a transient pressure distribution on the object's surface. In the case of small disturbances, the linearized equations of acoustics have been used successfully in many applications [10], in some occasions agreeing with experiments even in the case of considerable pressure amplitudes [4, 11].

Hudson [4] formulated a model based on sound pulse theory which captures the pressure clearing in the early stages of a shock wave loading on a wall of finite size. A similar approach was published by Merritt [13], who treated waves of finite rise time. Neither of these models, however, is able to predict the loading for the case of considerable wave lengths compared to the object size, for the following reasons: (i) Hudson's model only considers the diffraction of the shock front; (ii) both models neglect inertial flow; (iii) both models assume that the wave reflection is independent of the setup of an inertial flow [4]. Both authors state that the range of applicability of their models is limited to very small ratios of wavelength to object size [4, 13]. To formulate a more versatile model, we extend the model developed by Merritt [13] to the case of longer wavelengths.

Figure 4 shows a schematic of the reflection-diffraction process of a pressure wave by a rectangular solid body. The wave reflections from the ground (compare Fig. 1) are treated by mirroring the body about the ground plane and accounting for diffracted waves emanating from the corners of the mirrored object. In order to capture the diffraction of variable wave shapes and lengths, it is necessary to continuously track the multiple diffracted waves from all four

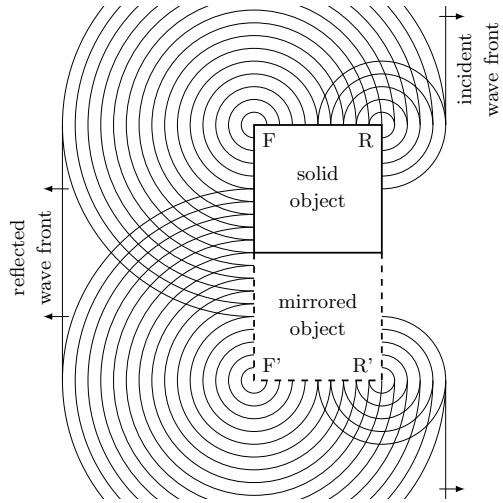

Figure 4: Diffraction of a wave around a rectangular object. Due to ground reflection, mirroring the object yields an identical problem.

corners. Friedlander has published an analytical solution [36, 37], based on Sommerfeld's theory of diffraction [9], of the diffraction of a pressure pulse around a right-angled wedge. When an incoming pressure wave causes a history $\tilde{p}_{\text{corner}}$ at a free edge ($r = 0$), the pressure due to the diffraction of the incoming wave on the object surface reads [13, 37]

$$\begin{aligned}
\tilde{p}_{\text{diff}}(c_0 t) &= \int_0^{\infty} \tilde{p}_{\text{corner}}\left(c_0 t - r\cosh(b)\right) q'_{\text{diff}}(b)\,\mathrm{d}b \\
&= \left[\tilde{p}_{\text{corner}}\left(c_0 t - r\cosh(b)\right) q_{\text{diff}}(b)\right]_0^{b_2} + \int_0^{b_2} \tilde{p}'_{\text{corner}}\left(c_0 t - r\cosh(b)\right) q_{\text{diff}}(b)\,\mathrm{d}\left(r\cosh(b)\right) \\
&= \tilde{p}_{\text{corner}}(0)\, q_{\text{diff}}(b_2) + \int_0^{b_2} \tilde{p}'_{\text{corner}}\left(c_0 t - r\cosh(b)\right) q_{\text{diff}}(b)\,\mathrm{d}\left(r\cosh(b)\right) \\
&= \tilde{p}_{\text{corner}}(0)\, q_{\text{diff}}(b_2) + \int_r^{c_0 t} \tilde{p}'_{\text{corner}}\left(c_0 t - \xi\right) q_{\text{diff}}(\xi/r)\,\mathrm{d}\xi.
\end{aligned} \tag{10}$$

Here, $b_2 = \cosh^{-1}(c_0 t/r)$ is the variable relating the distance travelled by the wave (c_0 being the ambient speed of sound and t the time) to the distance from the free edge r and $\xi = r\cosh(b)$. We note that $\tilde{p}_{\text{diff}}$ and $\tilde{p}_{\text{corner}}$ are pressure functions in terms of $c_0 t$ and that $(\cdot)'$ denotes the derivative $\frac{\partial(\cdot)}{\partial(c_0 t)}$ in this context. The functions $p_{\text{corner}}(t)$ for the front (F) and rear (R) corners are calculated using the procedure described in Subsection 3.2.1 and transformed to $\tilde{p}_{\text{corner}}(c_0 t) = p_{\text{corner}}(t/c_0)$ for use in Eq. (10). The function q_{diff} is defined in [37] as

$$\begin{aligned}
&q_{\text{diff}}(b) = u(\theta_2) + u(\theta_2 + 3\pi) + u(-\theta_2) + u(-\theta_2 + 3\pi), \\
&q_{\text{diff}}(0) = 0, \\
&u(\theta_2) = -\frac{1}{\pi}\tan^{-1}\left(\frac{\sin\left(\frac{\pi}{3}\right)\sinh\left(\frac{\pi}{3}\right)}{\cos\left(\frac{\theta_1-\theta_2}{3}\right) - \cos\left(\frac{\pi}{3}\right)\cosh\left(\frac{b}{3}\right)}\right).
\end{aligned} \tag{11}$$

The angles θ_1 and θ_2 define the direction of propagation of the diffracted wave and the angle of incidence relative to the direction of the incident wave, respectively. Table 3 gives the values for θ_1 and θ_2 for the four different scenarios encountered during the diffraction of the incident wave (compare Fig. 4). Evaluating Eq. (10) for a step wave at

$c_0 t/r \to \infty$ shows that the maximum pressure amplitude of a diffracted wave is limited to either 1/3 or 2/3 of the incoming pressure. Secondary diffractions (diffraction of a diffracted wave) can be treated using the four cases given in Table 3.

As an example, the incident wave front diffracts at rear corner R, and the consequent diffracted wave encounters corner R', where a secondary diffraction wave originates. This wave encounters F' before arriving at the front surface again. The maximum pressure amplitude of this wave after three subsequent diffractions is thus $(2/3)^3 \approx 0.296$ of the incoming wave amplitude. In order to accurately estimate the transient pressure distributions for both short and long duration loading, we include in our model all diffraction processes with possible peak pressures of more than 5% of the incoming pressure amplitude.

Table 3: Four possible scenarios for normal diffraction of a planar wave at right angled corner: angles of incidence and propagation relative to the direction of the incident wave and maximum relative amplitude.

surface	diffraction at corner	$\theta_1[^\circ]$	$\theta_2[^\circ]$	$\frac{p_{\mathrm{diff}}}{p_{\mathrm{i}}}\left(\frac{c_0 t}{r} \to \infty\right)$
front	F	270	180	-2/3
top	F	0	180	1/3
top	R	0	0	-1/3
back	R	270	0	2/3

Equations (10) and (11) can readily be evaluated numerically for arbitrary incoming pressure waves. The wave reflection can be accounted for by multiplying the incident pressure on the front surface $p_{\mathrm{f}}(t)$ by the reflection coefficient

$$C_{\mathrm{r}}(t) = \frac{(3\gamma - 1)\,\frac{p_{\mathrm{f}}(t)}{p_0} + 4\gamma}{(\gamma - 1)\,\frac{p_{\mathrm{f}}(t)}{p_0} + 2\gamma}, \tag{12}$$

which varies between 2 and 8 under the assumption of air as perfect gas. As pointed out by Hudson [4], assuming that the wave reflection can, over the whole duration of the process, be treated as one-dimensional, will likely yield an overestimation of the pressure on the front surface. The increase of the reflection coefficient in the compressible regime over the acoustic value of two is due to an abrupt deceleration of the particles incident on a rigid surface [8]. However, if the surface is finite, a flow around the object is established after sufficient time; particles evade the object, rather than being brought to rest at its surface. In order to account for this effect, a 'fade out' function is introduced as

$$C_{\mathrm{r,fade}}(t) = \begin{cases} C_{\mathrm{r}}(t) - \frac{C_{\mathrm{r}}(t)-2}{t_{\mathrm{fade}}} t, & t < t_{\mathrm{fade}}, \\ 2, & t \geq t_{\mathrm{fade}}, \end{cases} \tag{13}$$

which linearly reduces the reflection factor to the acoustic value of two. The pressure due to reflection of the incident wave is therefore

$$p_{\mathrm{r}}(t) = C_{\mathrm{r,fade}}(t) p_{\mathrm{f}}(t). \tag{14}$$

The average pressures on the front and back surfaces due to reflection and diffraction thus read

$$\begin{aligned} \bar{p}_{\mathrm{f,diff}}(t) &= \frac{1}{H} \int_{y=0}^{H} p_{\mathrm{r}}(t, y) + \sum_{i=1}^{n_{\mathrm{front}}} p_{\mathrm{diff,front},i}(t, y)\,\mathrm{d}y, \\ \bar{p}_{\mathrm{b,diff}}(t) &= \frac{1}{H} \int_{y=0}^{H} \sum_{i=1}^{n_{\mathrm{back}}} p_{\mathrm{diff,back},i}(t, y)\,\mathrm{d}y, \end{aligned} \tag{15}$$

where $n_{\mathrm{front}} = n_{\mathrm{back}} = 28$ individual contributions due to multiple diffractions are considered. Equation (15) was evaluated at 100 time steps of equal length and the spatial averaging over the surfaces was accomplished by computing the average pressure over 20 points, placed at equal distance over the object height.

3.2.3. History force model

It is well established that a relative acceleration between a body and a surrounding fluid causes forces on the body (see e.g. [16]). Under the assumption of incompressible flow, these forces are often termed 'added-mass' forces and are proportional to the instantaneous relative acceleration between the fluid and the body as well as to the density of the accelerated fluid [21]. The geometry-dependent constant of proportionality can be derived from potential flow theory and has been shown to be independent of the Reynolds number for cylinders and spheres [19, 38, 39].

In compressible flow however, the concept of added-mass loses its significance. The finite speed of sound propagation changes both the amplitude and the time evolution of the forces exerted on the body; specifically, the instantaneous dependence on the force on the relative acceleration ceases to hold. Early work by Miles [16] and Longhorn [17] investigated the influence of compressibility on the force caused by relative acceleration between a fluid and a cylinder and sphere, respectively, in the acoustic limit. More recently, Parmar et. al [20] studied the influence of finite Mach numbers for both cylinders and spheres, and found a significant increase in amplitude and time delay of the maximum force with increasing Mach number. These authors reported unanimously that the force evolution occurs on the acoustic time scale L_c/c_0, with L_c being a characteristic length of the body, rather than instantaneously as in the incompressible case [16, 17, 20]. In accordance with Parmar et. al [15] we refer to the force contribution discussed here as 'history force'. In this study we will adapt the results published by Parmar et. al [20] to obtain an estimate for the force contribution on a rectangular object due to flow acceleration.

The history force on a rectangular object, as defined in Fig. 1, has only been investigated for incompressible flow so far. However, for a two-dimensional flat plate, potential flow theory yields an added-mass coefficient identical to that of a circular cylinder [40]. For this reason we adopt the previously published results for circular cylinders [20] to approximate the history force term on a rectangular object, and define the history force contribution as

$$\boldsymbol{F}_{\mathrm{hist}}(t) = -\int_{-\infty}^{t} K\left(c_0(t-\chi)/H; M\right) \frac{\mathrm{d}(m_{\mathrm{df}}\boldsymbol{v})}{\mathrm{d}t}\, \mathrm{d}\left(\frac{c_0\chi}{H}\right). \tag{16}$$

In Eq. (16), K denotes Mach number dependent Kernel functions which were published by Parmar et. al [20]. The quantities $m_{\mathrm{df}} = m_{\mathrm{df}}(t)$ and $\boldsymbol{v} = \boldsymbol{v}(t)$ denote the time dependent mass of the displaced fluid and the undisturbed particle velocity of the incident flow, respectively. The object height H was chosen as characteristic length scale, in accordance with Section 2.

The kernel functions K hold for small relative accelerations from an initially steady and fully developed subcritical flow. This implies that the Mach number is assumed as constant and smaller than the critical value for the evaluation of Eq. (16). However, in the problem at hand the fluid is at rest before the pressure wave arrives at the structure, and the effective particle velocity and Mach number of the flow around the object can vary from zero to high values very quickly. Moreover, with wide ranges of the non-dimensional parameters (3) being investigated in this study, cases with large object dimensions compared to the incident wave length need to be considered, and a description of the total force as in Eq. (16) might be inapplicable. We therefore apply the following modifications to Parmar's history force model [15]:

1. Instead of computing the force directly as in equation (16), an average front and back pressure due to the acceleration reaction is calculated.
2. The force kernel is adapted to account for the change in Mach number. For flow Mach numbers exceeding the critical value of a circular cylinder (approximately 0.4), the Kernel for the highest available Mach number, $M = 0.39$, is used. Due to the change of the Kernel function, the convolution integral in Eq. (16) needs to be evaluated numerous times. However, it was found sufficient to compute average Mach numbers of 20 equally long time intervals and to evaluate Eq. (16) anew for these.
3. Both front and back pressure due to the acceleration reaction are multiplied by a 'fade-in' function to account for the initial set up of an inertial flow.
4. The front and back pressure are averaged over a short period of time, $\Delta t_{\mathrm{avg,hist}}$, to account for the time to change the flow conditions around the structure.

The changes in front and back pressure due to the flow acceleration are thus computed as

$$\begin{aligned}\bar{p}_{\mathrm{f,hist}}(t) &= \beta(t)\frac{1}{\Delta t_{\mathrm{avg,hist}}}\int_{t-\Delta t_{\mathrm{avg,hist}}}^{t}\frac{1}{H}\int_{-\infty}^{\tilde{t}} K\left(\frac{c_0(\tilde{t}-\chi)}{H};M_{\mathrm{f}}\right)\frac{\mathrm{d}(m_{\mathrm{df,f}}v_{\mathrm{f}})}{\mathrm{d}\tilde{t}}\,\mathrm{d}\left(\frac{c_0\chi}{H}\right)\mathrm{d}\tilde{t},\\ \bar{p}_{\mathrm{b,hist}}(t) &= -\beta(t)\frac{1}{\Delta t_{\mathrm{avg,hist}}}\int_{t-\Delta t_{\mathrm{avg,hist}}}^{t}\frac{1}{H}\int_{-\infty}^{\tilde{t}} K\left(\frac{c_0(\tilde{t}-\chi)}{H};M_{\mathrm{b}}\right)\frac{\mathrm{d}(m_{\mathrm{df,b}}v_{\mathrm{b}})}{\mathrm{d}\tilde{t}}\,\mathrm{d}\left(\frac{c_0\chi}{H}\right)\mathrm{d}\tilde{t},\end{aligned} \tag{17}$$

with $m_{\mathrm{df,f}} = m_{\mathrm{df,b}} = \rho(t)\pi H^2/4$ and $\beta(t)$ denoting a fade-in function, defined as

$$\beta(t) = \begin{cases}\frac{t}{t_{\mathrm{fade}}}, & t < t_{\mathrm{fade}},\\ 1, & t > t_{\mathrm{fade}}.\end{cases} \tag{18}$$

The subscripts 'f' and 'b' refer to evaluation of a quantity at the front and back surface, respectively, using the procedure described in Subsection 3.2.1. We note that Eq. (17) implies the assumption that the force defined in Eq. (16) is due to equal pressure amplitudes on the front and back surfaces. The evaluation of Eq. (17) can be performed numerically, assuring a sufficiently small time step to sample the force kernels K and the wave shape. This was assured by limiting the time step to a one-hundredth of the wave duration and by sampling the non-zero portion of the force kernel with at least 150 points.

3.2.4. Quasi-steady force model

When a body is immersed in a steady flow it experiences a drag force which is dependent on body shape, Reynolds number and Mach number. Various authors have reported these correlations for many different object shapes. In this context we adopt values reported in two classical textbooks on the subject [41, 42].

1. Dependence on Reynolds number: the sharp edges of the rectangular body induce flow separation regardless of the Reynolds number, thus the Reynolds number loses its influence above $Re > 10^4$. In the context of this study we therefore neglect the influence of the Reynolds number on the drag coefficient.
2. Dependence on object shape: The dependence of the drag coefficient on the aspect ratio W/L of a rectangular body is taken from [41], except for the value at $W/L \to 0$ which is taken from [42], and given in Table 4. Hereby, L denotes the side length of the rectangle normal to the incoming flow. With the assumption of symmetry around the middle axis and neglecting the influence of the ground boundary layer, we infer $c_{\mathrm{D}}(W/L) = c_{\mathrm{D}}(W/H)$.
3. Split in average front and back pressure: Hoerner [42] reports the split of the drag coefficient for a flat, two-dimensional plate in incompressible flow as $c_{\mathrm{D}} = c_{\mathrm{p,f}} - c_{\mathrm{p,b}} = 0.85 + 1.13 = 1.98$. We adopt this splitting by assuming that, with changing the aspect ratio $\bar{W}$, only the back pressure coefficient changes according to $c_{\mathrm{p,b}}\left(\bar{W}\right) = c_{\mathrm{p,f}} - c_{\mathrm{D}}\left(\bar{W}\right)$, which is equivalent to neglecting the contribution of viscous forces on the top surface to the overall drag coefficient.
4. Dependence on Mach number: A simple model for the change of drag due to subsonic compressibility is given by Hoerner [42]. It is assumed that only the front pressure changes due to the increase in stagnation pressure over the incompressible value and thus a Mach number dependent front pressure coefficient can be defined as

$$\tilde{c}_{\mathrm{p,f}}\left(M_{\mathrm{f}}\right) \approx c_{\mathrm{p,f}}\left(1 + \frac{M_{\mathrm{f}}^2}{4}\right) = 0.85\left(1 + \frac{M_{\mathrm{f}}^2}{4}\right). \tag{19}$$

   This model holds for subsonic, subcritical flow only (approximately $M < 0.8$ for $\bar{W} = 1$ [42]).

The average front and back pressures can thus be written as

$$\begin{aligned}\bar{p}_{\mathrm{f,qs}}(t) &= \frac{1}{\Delta t_{\mathrm{avg,qs}}}\int_{t-\Delta t_{\mathrm{avg,qs}}}^{t}\frac{1}{2}\tilde{c}_{\mathrm{p,f}}\rho_{\mathrm{f}}{v_{\mathrm{f}}}^2\,\mathrm{d}\tilde{t},\\ \bar{p}_{\mathrm{b,qs}}(t) &= \frac{1}{\Delta t_{\mathrm{avg,qs}}}\int_{t-\Delta t_{\mathrm{avg,qs}}}^{t}\frac{1}{2}c_{\mathrm{p,b}}\rho_{\mathrm{b}}{v_{\mathrm{b}}}^2\,\mathrm{d}\tilde{t}.\end{aligned} \tag{20}$$

Similar to Eq. (17), the pressures are averaged over a small amount of time, $\Delta t_{\mathrm{avg,qs}}$, to account for the inertia of the flow field around the object.

Table 4: Dependence of drag coefficient on the aspect ratio of a rectangular object for $Re > 10^4$ [41, 42].

W/L	0.0	0.1	0.2	0.4	0.5	0.65	0.8	1.0	1.2	1.5	2.0	2.5	3.0	6.0
c_{D}	1.98	1.98	2.1	2.35	2.5	2.9	2.3	2.2	2.1	1.8	1.6	1.4	1.3	0.89

3.2.5. Complete model and empirical factors

The three contributions to the overall drag force per unit width (9) add to give

$$\begin{aligned} F(t) &= F_{\mathrm{diff}}(t) + F_{\mathrm{hist}}(t) + F_{\mathrm{qs}}(t) \\ &= H\left(\bar{p}_{\mathrm{f,diff}}(t) - \bar{p}_{\mathrm{b,diff}}(t) + \bar{p}_{\mathrm{f,hist}}(t) - \bar{p}_{\mathrm{b,hist}}(t) + \bar{p}_{\mathrm{f,qs}}(t) - \bar{p}_{\mathrm{b,qs}}(t)\right). \end{aligned} \tag{21}$$

The empirical factors $t_{\mathrm{fade}}, \Delta t_{\mathrm{avg,hist}}, \Delta t_{\mathrm{avg,qs}}$, introduced in Eqs. (13), (17), and (20) were determined by comparison to numerical predictions as

$$t_{\mathrm{fade}} = 10\frac{H}{c_0}, \qquad \Delta t_{\mathrm{avg,hist}} = 2\frac{H}{c_0}, \qquad \Delta t_{\mathrm{avg,qs}} = 5\frac{H}{c_0}. \tag{22}$$

We note that all three empirical constants are on the acoustic time scale H/c_0, which is equal to the time a sound wave requires to sweep the front or back surface of the object.

3.3. Validation of the analytical model

The analytical model introduced above is now validated by comparing predicted pressure histories to those obtained via CFD simulations.

3.3.1. Detailed comparison of pressure loading histories

Four selected cases were chosen to compare the two sets of predictions and to illustrate the different contributions to the load, as defined in Eq. (21). In Fig. 5a-f we present the results for the first two cases, which are of complementary nature. Figs. 5a-c show the results for the case of a shock wave ($\alpha_{\mathrm{r}} = 0$) of short duration ($\tau_{\mathrm{i}} = 1$) and high amplitude ($\bar{p}_{\mathrm{i}} = 3$) passing over a thin object ($\bar{W} = 0.1\bar{W}_0$). It can be seen in Figs. 5a and 5c that CFD and analytical model are in good agreement in terms of pressure on the front surface and overall force on the object. Some discrepancies in the history of the average back pressure are apparent from Fig. 5b. This can be attributed to the high pressure ratio producing locally supersonic flow and giving rise to complex flow phenomena around the rear corner. Due to the low amplitude of the pressure on the back of the object compared to the front surface, the influence of this discrepancy on the overall force is of small significance. As evident from Fig. 5c, the loading of the object is dominated by wave diffraction in this case.

In Figs. 5d-f, a loading scenario of the other extreme is shown. In this case the wave length is two orders of magnitude greater than the object height, together with a significant rise time ($\alpha_{\mathrm{r}} = 0.5$). According to Fig. 5f, the quasi-steady contribution is clearly the dominant contribution, as pressure on front and back of the surface due to diffraction have enough time to equilibrate. Excellent agreement is found between CFD and analytical results in terms of front pressure and force history. While the general trend of the back pressure is well represented by the analytical model, the CFD model captures the effects of transient vortex shedding, which give rise to an oscillatory back pressure evolution, not accounted for by the analytical model.

In Fig. 5g-l we compare the results of CFD and analytical model for two cases which only differ in the rise time coefficient α_{r}. We observe once again excellent agreement in terms of front pressure, back pressure, and total force on the object for both cases. Comparing Figs. 5g-i to 5j-l we find that the finite rise time significantly changes the amplitude of the overall force, which can be attributed to the so-called clearing effect, i.e. rarefaction waves alleviate the pressure on the forward facing surface. While diffraction and reflection dominate the pressure on the front surface, significant contributions to the back pressure are made by quasi-steady and history effects, giving rise to non-negligible force contributions, observed in Figs. 5i and 5l.

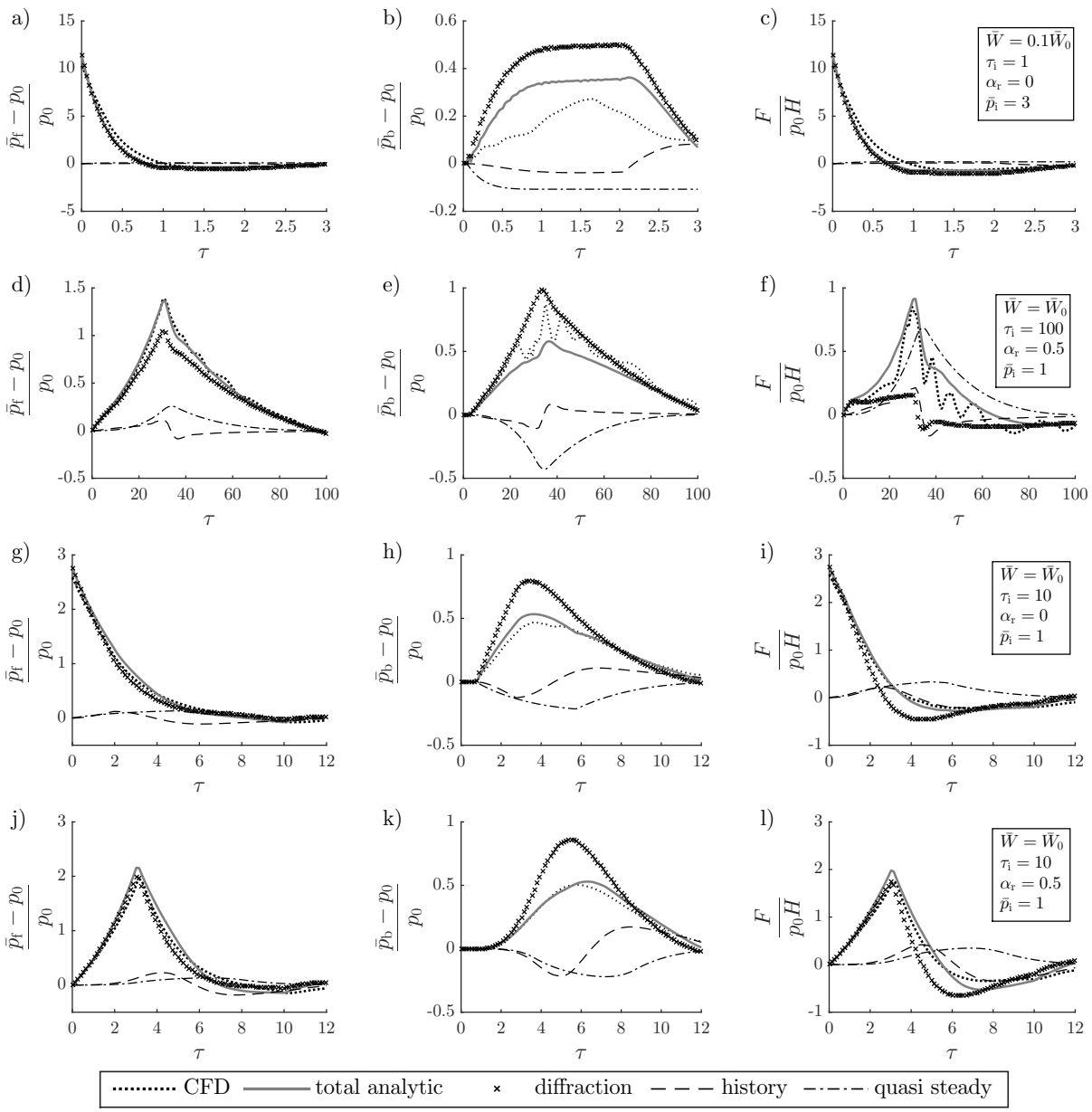

Figure 5: Comparison of the average pressure on front and back surface and the total force obtained with CFD and the analytical model. The contributions of the analytically obtained pressures are shown.

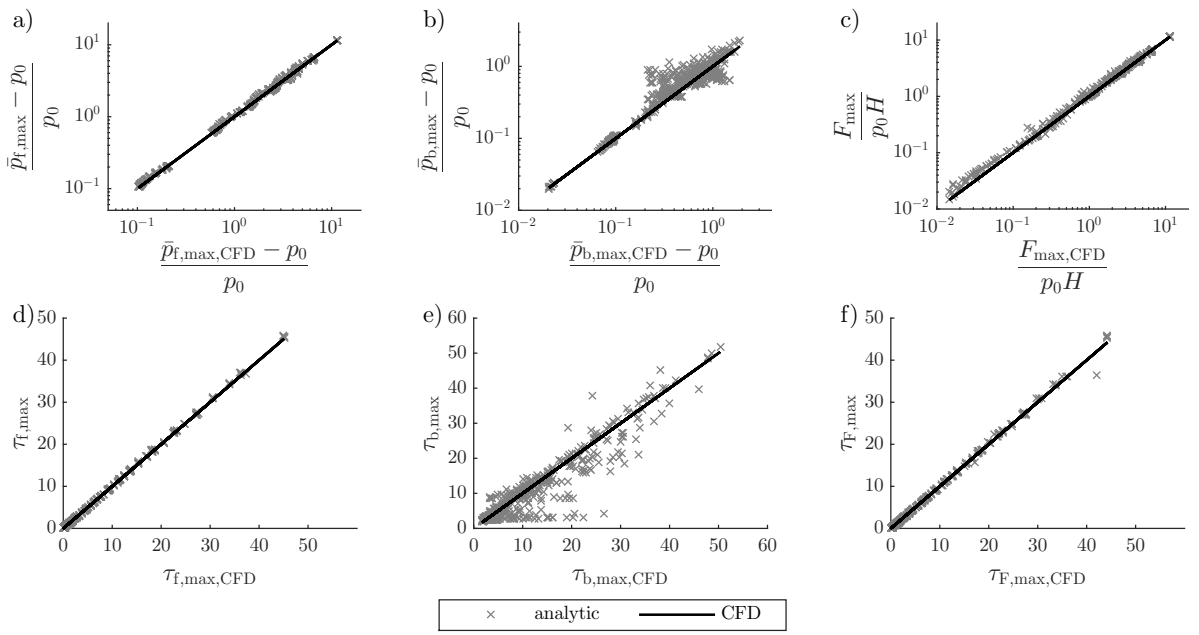

Figure 6: Correlations between CFD results and analytical results for the maximum pressures and time to maximum pressure on front and back surface and the pressure differential.

3.3.2. Correlation between CFD and analytical model

We proceed by considering the maximum average pressure on the front and back surfaces, $\bar{p}_{\mathrm{f,max}}$ and $\bar{p}_{\mathrm{b,max}}$, respectively, and the maximum net force on the object, $F_{\max}$, as well as the non-dimensional times at which these values are reached, namely $\tau_{\mathrm{f,max}}$, $\tau_{\mathrm{b,max}}$, $\tau_{F,\max}$. The parametric space defined in (8) was explored to compare the analytical and numerical predictions.

In Fig. 6 we present the comparison of the two sets of predictions. Figs. 6a and 6d refer to the pressure loading on the front surface, and show excellent agreement of the two sets of predictions, across all cases. Figures 6b and 6e refer to loading on the back surface. The sharp rear corner gives rise to various complex flow phenomena like vortex roll up, vortex shedding, and wave diffraction under the influence of compressibility, which cannot be captured in detail by the relatively simple analytical model. However, the estimate of the back pressure is of sufficient accuracy to yield good agreement in terms of maximum force on the object, as illustrated in Figs. 6c and 6f. The analytical model tends to slightly overestimate the maximum force, and force estimates are therefore likely to be conservative.

4. Results and discussion

Prior work has investigated the pressure on a finite surface loaded by an incoming shock wave [4] or very short rise time wave [13], as well as the forces on particles in unsteady flow [15]. However, for considerable rise time of the pressure wave, as encountered in accidental deflagration events, the loading on objects of different sizes cannot be captured by any of the previously published models. In industrial practice design engineers currently rely on existing models [7], even if their accuracy is known to be low outside their range of validation. The models proposed here improve the design process considerably.

4.1. CFD predictions

In the following we present the maximum average pressure on front and back surface as well as the maximum differential pressure or net force on the object for wide ranges of the non-dimensional parameters governing the problem (3). In order to characterise the transient nature of the loading, we also record the time taken to reach maximum load. We have chosen to present average pressures over the surfaces, as in practice the assumption of

uniform loading is often made for design purposes. In Fig. 7a the maximum average pressure on the front surface is plotted over the inverse of a Strouhal number in terms of pressure, defined as

$$St_p = \frac{p_\mathrm{i} + p_0}{\alpha_\mathrm{r}\tau_\mathrm{i} p_0} = \frac{H/c_0}{\alpha_\mathrm{r} t_\mathrm{i}} \frac{p_\mathrm{i} + p_0}{p_0}. \tag{23}$$

This dimensionless number is a measure for the degree of unsteadiness of the problem at hand, comparing the rise time of the pressure wave to the time a sound wave needs to sweep the height of the object, multiplied by the ratio of maximum incoming pressure to ambient pressure.

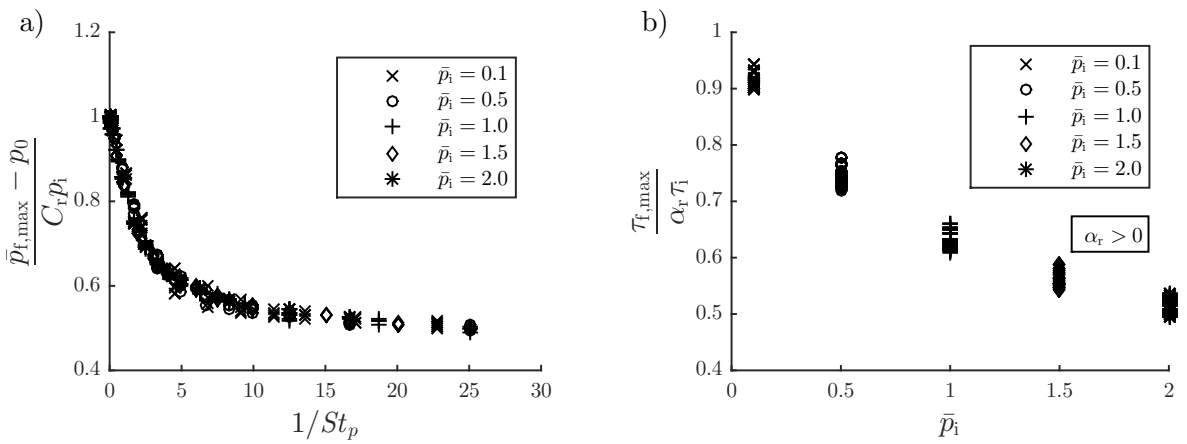

Figure 7: Variation of the maximum average pressure on the front surface with the Strouhal number (a) and time to maximum average pressure on the front surface for cases with $\alpha_\mathrm{r} > 0$ (b), as predicted by CFD.

As can be seen in Fig. 7a, employing this scaling and normalising overpressures by the theoretical value obtained for the case of one-dimensional reflection results in clustering of the data points. It is evident from Fig. 7a that short rise times and higher pressure ratios promote maximum front pressure loads closer to the maximum theoretical value of $C_\mathrm{r} p_\mathrm{i}$. We note that in theory, slightly higher values are possible for small non-zero rise times and considerable overpressures, due to higher reflection coefficients for isentropic compression (see e.g. [43]). With decreasing Strouhal number, the maximum pressure rapidly decreases before flattening out for high values of $1/St_p$, seemingly approaching a value of half the theoretical maximum. This behaviour can be explained by the emergence of rarefaction waves from the free edges of the body in the very early stages ('clearing') and the development of an inertial flow around the body later on, which decreases the severity of the initial wave reflection.

In Fig. 7b we present the time to maximum load on the front surface as a function of the amplitude of the incoming wave. It can be seen that the arrival time of the average pressure peak on the front surface, denoted by $\tau_\mathrm{f,max}$, decreases with increasing pressure ratio as a consequence of increasingly strong compressibility effects; as the wave reflects from the surface, a region of high pressure and temperature emerges, giving rise to additional wave distortion.

Figure 8a shows the maximum load, F_max, for an aspect ratio of $\bar{W} = \bar{W}_0$, as a function of the rise time $\alpha_\mathrm{r}\tau_\mathrm{i}$, leading to data points grouped by overpressure ratio. It can be seen that the maximum force decreases with increasing rise time, asymptotically approaching a value depending on the overpressure ratio.

In Fig. 8b the time to reach the maximum force is plotted versus the pressure ratio, showing similar behaviour to Fig. 7b, and indicating that the maximum net load on the object is reached at a similar time as the maximum front surface load.

Having established the behaviour of the maximum force with changing rise time $\alpha_\mathrm{r}\tau_\mathrm{i}$ for one aspect ratio and multiple pressure ratios, in Fig. 9 we present a design map to predict the maximum load on an object for three different aspect ratios. From this figure the maximum net force on a structure can be extracted without any further calculation. Knowledge of the characteristic of the incoming pressure wave allows identifying a point in the map, while knowledge of the aspect ratio allows identifying the right set of contours for the maximum force. It can be seen that the aspect ratio $\bar{W}$ has considerable influence on the maximum force experienced by the object. This is due to the

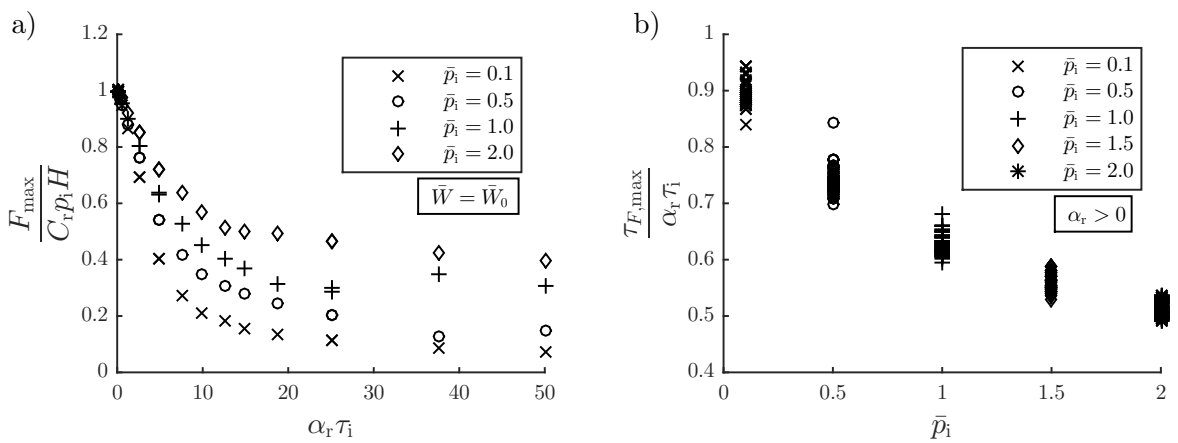

Figure 8: Variation of the maximum differential pressure with the wave rise time (a) and time to maximum differential pressure on the front surface for cases with $\alpha_\mathrm{r} > 0$ (b), as predicted by CFD.

increasing delay in the arrival time of the wave at the back surface and to the differences in the inertial flow field (e.g. flow reattachment for large aspect ratios).

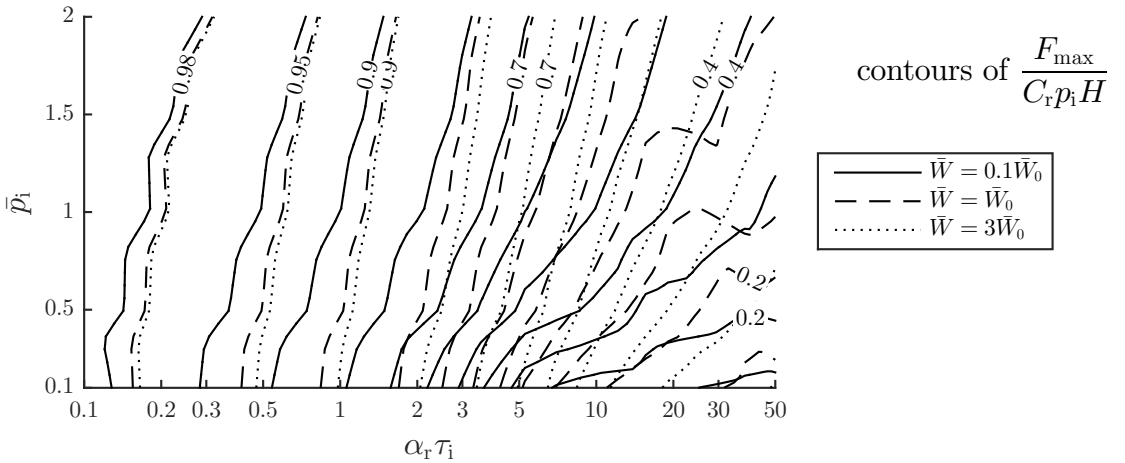

Figure 9: Contour plot of maximum force for three different aspect ratios, as predicted by CFD.

Next, we present the change of maximum average back pressure with wavelength τ_i for three different pressure ratios in Fig. 10. These figures can directly be used to determine the maximum load on the back surface of the object for given input parameters. The maximum recorded back pressure increases mostly monotonically with increasing wavelength before approaching an asymptotic value, which in none of the cases exceeds the incoming pressure. Interestingly, the maximum pressure is lower for higher pressure ratios when compared to the incoming value. This can be attributed to the high particle velocities and Mach numbers caused by high pressure ratios, which give rise to higher suction in the wake region of the body.

Figure 11 shows contours of maximum average back pressure for different overpressure and time durations. As the back pressure is not only a function of the rise time $\alpha_\mathrm{r}\tau_\mathrm{i}$, but of both duration τ_i and rise time coefficient α_r individually, we present maps for the two cases $\alpha_\mathrm{r} = 0$ and $\alpha_\mathrm{r} = 0.5$. A pronounced effect of the aspect ratio can be observed in both Fig. 11a and 11b. It can be seen that high durations promote higher back pressure values for all aspect ratios. From this figure the maximum net force on a structure can be extracted without any further calculation. Knowledge of the characteristic of the incoming pressure wave allows identifying a point in the map, while knowledge

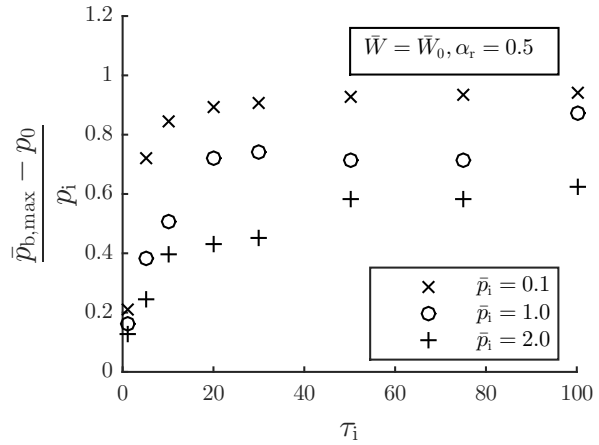

Figure 10: Variation of maximum pressure on the back surface with wave length and pressure ratio, as predicted by CFD.

of the aspect ratio allows identifying the right set of contours for the maximum force.

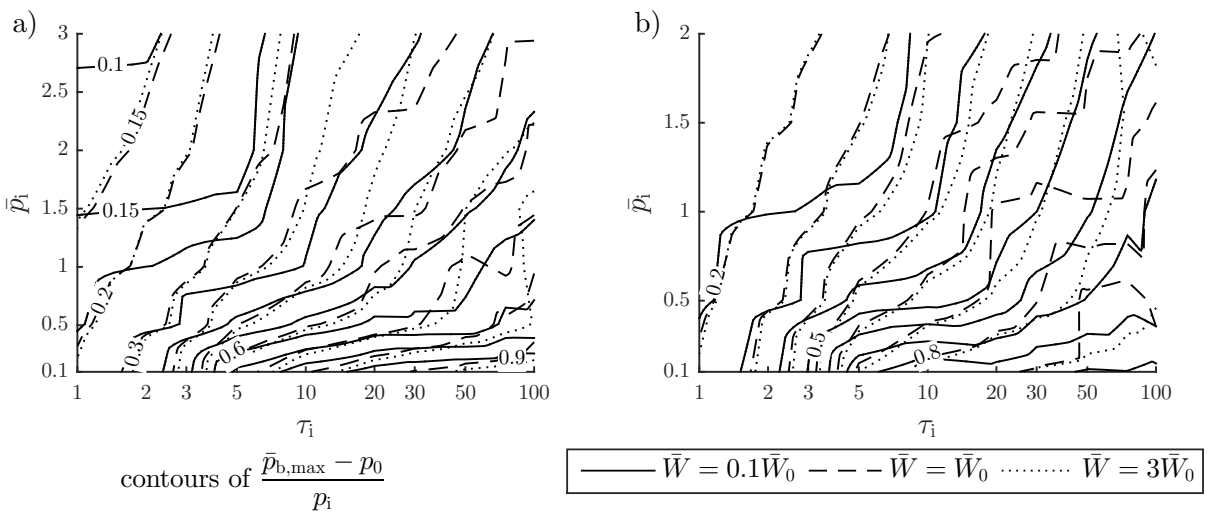

Figure 11: Contour plot of maximum back pressure for three different aspect ratios for $\alpha_r = 0$ (a) and $\alpha_r = 0.5$ (b), as predicted by CFD.

The time to maximum back pressure can be estimated as

$$\tau_{b,max} = \left(\alpha_r \tau_i + \bar{W}\right) \frac{U_{max}}{c_0} + 2, \tag{24}$$

where U_{max} is the propagation velocity of the pressure peak of the incoming wave. Equation (24) assumes the maximum of the back face loading to appear at the instant when the diffracted wave at the rear corner has swept the back face twice. Comparing Eq. (24) to CFD results showed that this equation consistently underestimates the time to maximum back face loading.

4.2. Analytical predictions

A very large parametric study including over 7000 cases was conducted, exploring beyond the space defined in (8). We use this large data set to explore in detail the predictions of the analytical model focussing on asymptotic behaviour of the loading.

Firstly, we examine the asymptotic value of maximum average pressure on the front surface, given in Fig. 12. As compared to Fig. 7a, we have chosen to normalise the front pressure by the stagnation pressure. We note that $\tilde{c}_{\mathrm{p,f}}$ is dependent on the maximum Mach number of the incoming wave M_{i} (see Appendix A), as defined in Eq. (19). From this diagram we can identify the stagnation pressure as an approximate asymptotic value for $1/St_p \rightarrow \infty$. In fact as early as $1/St_p = 50$, the maximum value of the maximum pressure lies within 10% of the stagnation pressure and for $1/St_p > 100$ the stagnation pressure can serve as a conservative estimate. This agrees well with the findings of other researchers concerning the asymptotic pressure caused by shock waves on small targets [44].

In Fig. 13 we present contours of the maximum force normalised by the maximum theoretical force or by the maximum quasi-steady drag due to the particle velocity in the incoming wave. We note that the drag coefficient $\tilde{c}_{\mathrm{D}}$ is defined as a function of Mach number and aspect ratio

$$\tilde{c}_{\mathrm{D}} = \tilde{c}_{\mathrm{p,f}}\left(M_{\mathrm{i}}\right) - c_{\mathrm{p,b}}\left(\bar{W}\right), \tag{25}$$

with $\tilde{c}_{\mathrm{p,f}}$ and $c_{\mathrm{p,b}}$ as defined in Eq. (19) and Table 4. Figure 13 suggests that for $\alpha_{\mathrm{r}}\tau_{\mathrm{i}} < 1$ the maximum theoretical force $C_{\mathrm{r}}p_{\mathrm{i}}H$ is a good estimate of the maximum structural load, whereas for $\alpha_{\mathrm{r}}\tau_{\mathrm{i}} > 100$, the load is within 10% of the corresponding steady state drag load, except for very small overpressure ratios. In case of very small overpressure ratios, the quasi-steady force plays only a minor role even for very long wavelengths, as the particle velocities become negligible. Similar behaviour was found for other aspect ratios than $\bar{W} = \bar{W}_0$.

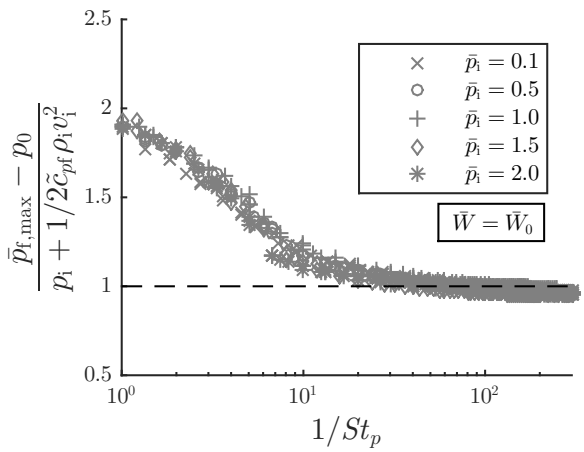

Figure 12: Maximum average front pressure values obtained with the analytical model to the steady front pressure value due to pure quasi-steady drag.

In Fig. 14 we present 'slices' through the contour plot shown in Fig. 13. In Fig. 14a we observe the transition between a single asymptotic value $C_{\mathrm{r}}p_{\mathrm{i}}H$ for low $\alpha_{\mathrm{r}}\tau_{\mathrm{i}}$ to a pressure ratio specific asymptote for large $\alpha_{\mathrm{r}}\tau_{\mathrm{i}}$. Fig. 14b illustrates the approximate convergence of the maximum structural load to the value $1/2\tilde{c}_{\mathrm{D}}\rho_{\mathrm{i}}{v_{\mathrm{i}}}^2H$ corresponding to steady state drag. It can be seen that only the lowest pressure ratio of $\bar{p}_{\mathrm{i}} = 0.1$ significantly deviates from this value, which is due to the reasons given above.

Finally, we examine the significance of the three force contributions, as defined in Eq. (9), for large ranges of input parameters. In Fig. 15 the relative importance of these contributions is shown for changing non-dimensional rise time $\alpha_{\mathrm{r}}\tau_{\mathrm{i}}$. We note that this graph includes data for the whole range of examined aspect ratios $\bar{W}$ and for pressure ratios $\bar{p}_{\mathrm{i}} \geq 0.5$. We therefore obtain ranges of relative importance, which are indicated by the lighter lines in Fig. 15, as well as mean values (heavier lines). We observe the anticipated behaviour of pure diffraction (and reflection) loading in the $\alpha_{\mathrm{r}}\tau_{\mathrm{i}} \rightarrow 0$ limit, and quasi-steady loading in the $\alpha_{\mathrm{r}}\tau_{\mathrm{i}} \rightarrow \infty$ limit. Moreover, the history force is found to have a significant influence for intermediate rise times of approximately $5 < \alpha_{\mathrm{r}}\tau_{\mathrm{i}} < 50$. Therefore, except for the extreme cases, all three force contributions need to be considered to accurately estimate the total force on an object.

The results presented in this section shed light on the nature of loading due to pressure waves of variable shape and duration. It has been shown that diffraction dominates the loading for rise times approaching zero, and that for

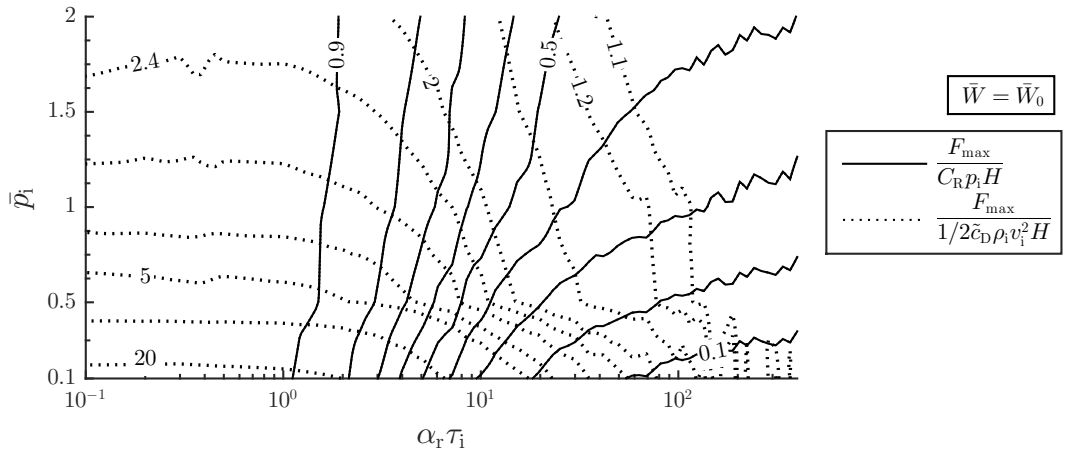

Figure 13: Contour plot of the maximum force obtained with the analytical model in two different normalisations.

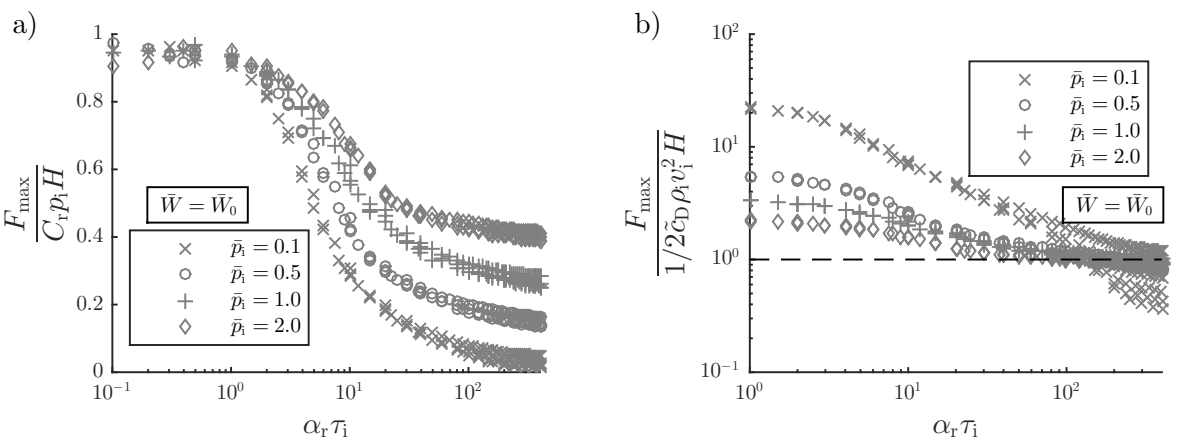

Figure 14: Maximum force obtained with the analytical model normalised by the theoretical maximum (a) and by the corresponding steady state drag (b).

increasingly large rise times the load progressively resembles the steady-state drag load for the same particle velocity. However, for a wide range of parameters in between these extremes, the load depends on all problem parameters and all three force contributions can have significant influence. The maps and equations presented in this section allow estimating the loading history on an arbitrary box-like object.

The analyses performed here are two-dimensional, hence representative of structures of depths much larger than their other two dimensions (neglecting three-dimensional flow effects). However, the loads obtained for the two-dimensional case can be used as upper bounds to the loads for a structure of finite width, as the finite width of an object promotes the clearing effect through additional rarefaction waves from the side edges. Moreover, steady-state drag coefficients are, in general, lower in the three-dimensional case as the flow can evade the structure more easily. Future work will investigate the effect of finite width on transient loads on objects, extending both the numerical and the analytical modelling approach to the three-dimensional case.

5. Conclusion

We have developed CFD simulations and an analytical model to predict the transient loading exerted on solid rectangular objects by pressure waves of arbitrary shape, amplitude and duration. The analytical modelling approach

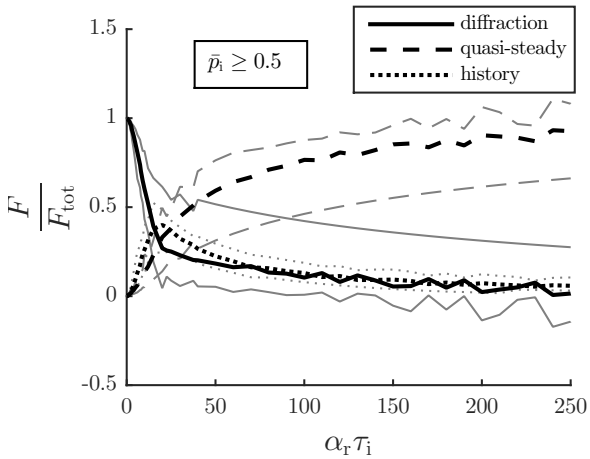

Figure 15: Force decomposition in diffraction, quasi-steady and history contributions. The lighter lines indicate upper and lower bounds of the included cases, the heavier lines represent the mean value for a specific rise time $\alpha_\mathrm{r}\tau_\mathrm{i}$ for $\bar{W} = 0.1\bar{W}_0 - 3\bar{W}_0$ and $\bar{p}_\mathrm{i} = 0.5 - 2$.

was validated using the more detailed numerical simulations, and the model's asymptotic behaviour was explored. The main conclusions of this study are as follows

- A predictive tool was developed to allow estimates of loading histories of box-like objects loaded by arbitrary pressure waves; design charts and design formulae were constructed to facilitate these estimates.
- The maximum load on a box-like structure by pressure wave loading is mainly governed by only two non-dimensional parameters, namely the non-dimensional rise time $\alpha_\mathrm{r}\tau_\mathrm{i}$ and the overpressure ratio $\bar{p}_\mathrm{i}$.
- It was shown that for very short non-dimensional rise times the loading is dominated by diffraction, while for intermediate rise times all three force contributions, including the history force, are significant.

Data accessibility. The raw data presented in the figures is available at doi:10.5061/dryad.17rf591.

Funding. The research was funded by the Turbomachinery Engineering team of Baker Hughes, a GE Company (BHGE - https://www.bhge.com/). We are grateful to M. Ruggiero for managing the financial side of the project.

Appendix A

At $t = 0$, the given triangular pressure wave implies a distribution in terms of overpressure $p = p_\mathrm{abs} - p_0$

$$p(\zeta) = \begin{cases} \frac{p_\mathrm{i}}{\alpha_\mathrm{r} t_\mathrm{i} c_0}\zeta, & 0 \leq \zeta \leq \alpha_\mathrm{r} t_\mathrm{i} c_0, \\ \frac{p_\mathrm{i}}{t_\mathrm{i}(1-\alpha_\mathrm{r})c_0}(t_\mathrm{i} c_0 - \zeta), & \alpha_\mathrm{r} t_\mathrm{i} c_0 < \zeta \leq t_\mathrm{i} c_0, \\ 0, & \text{else}, \end{cases} \tag{A.1}$$

where ζ is a spatial coordinate pointing from the wave front to the wave tail, with $\zeta = 0$ at the wave front, i.e. $\zeta = -x$ (compare Fig. 2a). For the case of a negligible rise coefficient $\alpha_\mathrm{r} = 0$, the pressure wave is a shock wave and the

properties behind the shock front are determined by the Rankine-Hugoniot equations for a perfect gas (e.g. [35])

$$\begin{aligned} \rho_{\text{shock}} &= \rho_0 \frac{2\gamma + (\gamma+1)\frac{p_\text{i}}{p_0}}{2\gamma + (\gamma-1)\frac{p_\text{i}}{p_0}}, \quad & T_{\text{shock}} &= \frac{p_\text{i} + p_0}{R\rho_{\text{shock}}}, \\ v_{\text{shock}} &= \frac{\frac{p_\text{i}}{p_0}\sqrt{\frac{p_0}{\rho_0}}}{\sqrt{\frac{\gamma+1}{2}\frac{p_\text{i}}{p_0} + \gamma}}, & M_{\text{shock}} &= \frac{v_{\text{shock}}}{\sqrt{\gamma R T_{\text{shock}}}}. \end{aligned} \tag{A.2}$$

Further behind the shock front it can be assumed that the gas undergoes isentropic expansion

$$\frac{p}{\rho^\gamma} = \text{const.} \tag{A.3}$$

and therefore the density, temperature and velocity fields can be calculated as [35]

$$\begin{aligned} \rho(\zeta) &= \rho_{\text{shock}} \left(\frac{p(\zeta)}{p_\text{i} + p_0} \right)^{1/\gamma}, & T(\zeta) &= \frac{p(\zeta)}{\rho(\zeta) R}, \\ v(\zeta) &= v_{\text{shock}} - \frac{2}{\gamma - 1} \left(\sqrt{\gamma R T_{\text{shock}}} - \sqrt{\gamma R T(\zeta)} \right), & M(\zeta) &= \frac{v(\zeta)}{\sqrt{\gamma R T(\zeta)}}. \end{aligned} \tag{A.4}$$

Similarly, for the case of a non-negligible rise coefficientα_r, the density, temperature and velocity fields can be calculated as

$$\begin{aligned} \rho(\zeta) &= \rho_0 \left(\frac{p(\zeta)}{p_0} \right)^{1/\gamma}, & T(\zeta) &= \frac{p(\zeta)}{\rho(\zeta) R}, \\ v(\zeta) &= \frac{2}{\gamma - 1} \left(\sqrt{\gamma R T(\zeta)} - c_0 \right), & M(\zeta) &= \frac{v(\zeta)}{\sqrt{\gamma R T(\zeta)}}. \end{aligned} \tag{A.5}$$

References

[1] M. Sun, T. Saito, K. Takayama, H. Tanno, Unsteady drag on a sphere by shock wave loading, Shock Waves 14 (1-2) (2005) 3–9. doi:10.1007/s00193-004-0235-4.

[2] H. Tanno, K. Itoh, T. Saito, A. Abe, K. Takayama, Interaction of a shock with a sphere suspended in a vertical shock tube, Shock Waves 13 (3) (2003) 191–200. doi:10.1007/s00193-003-0209-y.

[3] U.S. Department of the Army, Structures to resist the effects of accidental explosions, technical manual TM5-1300, Washington, DC, "https://www.wbdg.org/ffc/army-coe/technical-manuals-tm/tm-5-1300" (1990).

[4] C. C. Hudson, Sound pulse approximations to blast loading (with comments on transient drag), Report SC-TM-191-55-5, Sandia Corporation (1955).

[5] Det Norske Veritas, DNV-RP-C204: Design against accidental loads, "http://www.dnv.com" (2010).

[6] American Petroleum Institute, API RP 2FB - recommended practice for the design of offshore facilities against fire and blast loading, Washington, D.C. (2006).

[7] The Steel Construction Institute, FABIG TN 14 - design of low to medium rise buildings against external explosions, "www.fabig.com" (2018).

[8] R. Courant, Supersonic flow and shock waves, New York : Interscience, New York, 1948.

[9] A. Sommerfeld, Mathematische theorie der diffraction, Mathematische Annalen 47 (2) (1896) 317–374. doi:10.1007/BF01447273.

[10] F. G. Friedlander, Sound pulses, Cambridge University Press, Cambridge, 1958.
URL `https://books.google.co.uk/books?id=jSW7AAAAIAAJ`

[11] A. Tyas, J. A. Warren, T. Bennett, S. Fay, Prediction of clearing effects in far-field blast loading of finite targets, Shock Waves 21 (2) (2011) 111–119. doi:10.1007/s00193-011-0308-0.

[12] S. E. Rigby, A. Tyas, T. Bennett, J. A. Warren, S. Fay, Clearing effects on plates subjected to blast loads, Proceedings of the Institution of Civil Engineers: Engineering and Computational Mechanics 166 (3) (2013) 140–148. doi:10.1680/eacm.12.00010.

[13] M. L. Merritt, On the effect of slow rise times on the blast loading of structures, Report AFSWP-460, Sandia Corporation (1953).

[14] J. Magnaudet, I. Eames, The motion of high-reynolds-number bubbles in inhomogeneous flows, Annual Review of Fluid Mechanics 32 (2000) 659–708.

[15] M. Parmar, A. Haselbacher, S. Balachandar, Modeling of the unsteady force for shock-particle interaction, Shock Waves 19 (4) (2009) 317–329. doi:10.1007/s00193-009-0206-x.

[16] J. W. Miles, On virtual mass and transient motion in subsonic compressible flow, Quarterly Journal of Mechanics and Applied Mathematics 4 (4) (1951) 388–400. doi:10.1093/qjmam/4.4.388.

[17] A. L. Longhorn, The unsteady, subsonic motion of a sphere in a compressible inviscid fluid, Quarterly Journal of Mechanics and Applied Mathematics 5 (1) (1952) 64–81. doi:10.1093/qjmam/5.1.64.
[18] J. Magnaudet, J. Fabre, M. Rivero, Accelerated flows past a rigid sphere or a spherical bubble. part 1. steady straining flow, Journal of Fluid Mechanics 284 (1995) 97–135. doi:10.1017/S0022112095000280.
[19] E. J. Chang, M. R. Maxey, Unsteady flow about a sphere at low to moderate reynolds number. Part 2. Accelerated motion, Journal of Fluid Mechanics 303 (1995) 133–153. doi:10.1017/S0022112095004204.
[20] M. Parmar, A. Haselbacher, S. Balachandar, On the unsteady inviscid force on cylinders and spheres in subcritical compressible flow, Philosophical Transactions of the Royal Society A: Mathematical, Physical and Engineering Sciences 366 (1873) (2008) 2161–2175. doi:10.1098/rsta.2008.0027.
[21] G. K. Batchelor, An Introduction to Fluid Dynamics, Cambridge Mathematical Library, Cambridge University Press, Cambridge, 2000. doi:DOI: 10.1017/CBO9780511800955.
URL https://www.cambridge.org/core/books/an-introduction-to-fluid-dynamics/18AA1576B9C579CE25621E80F9266993
[22] H. L. Gauch, O. Lines, F. Montomoli, V. L. Tagarielli, Predictions of the transient loading on circular cylinders by arbitrary pressure waves in air, In Preparation.
[23] C. J. Greenshields, H. G. Weller, L. Gasparini, J. M. Reese, Implementation of semi-discrete, non-staggered central schemes in a colocated, polyhedral, finite volume framework, for high-speed viscous flows, International Journal for Numerical Methods in Fluids 63 (1) (2010) 1–21. doi:10.1002/fld.2069.
[24] H. G. Weller, G. Tabor, H. Jasak, C. Fureby, A tensorial approach to computational continuum mechanics using object-oriented techniques, Computers in Physics 12 (6) (1998) 620–631. doi:10.1063/1.168744.
[25] F. R. Menter, Two-equation eddy-viscosity turbulence models for engineering applications, AIAA Journal 32 (8) (1994) 1598–1605. doi:10.2514/3.12149.
[26] R. M. Stringer, J. Zang, A. J. Hillis, Unsteady RANS computations of flow around a circular cylinder for a wide range of reynolds numbers, Ocean Engineering 87 (2014) 1–9. doi:10.1016/j.oceaneng.2014.04.017.
[27] P. Meliga, G. Pujals, T. Serre, Sensitivity of 2-D turbulent flow past a D-shaped cylinder using global stability, Physics of Fluids 24 (6). doi:10.1063/1.4724211.
[28] G. Iaccarino, A. Ooi, P. A. Durbin, M. Behnia, Reynolds averaged simulation of unsteady separated flow, International Journal of Heat and Fluid Flow 24 (2) (2003) 147–156. doi:https://doi.org/10.1016/S0142-727X(02)00210-2.
[29] W. Rodi, Comparison of LES and RANS calculations of the flow around bluff bodies, Journal of Wind Engineering and Industrial Aerodynamics 69-71 (1997) 55–75. doi:https://doi.org/10.1016/S0167-6105(97)00147-5.
[30] A. Kurganov, E. Tadmor, New high-resolution central schemes for nonlinear conservation laws and convection-diffusion equations, Journal of Computational Physics 160 (1) (2000) 241–282. doi:10.1006/jcph.2000.6459.
[31] B. van Leer, Towards the ultimate conservative difference scheme. II. monotonicity and conservation combined in a second-order scheme, Journal of Computational Physics 14 (4) (1974) 361–370. doi:10.1016/0021-9991(74)90019-9.
[32] P. J. Roache, Perspective: A method for uniform reporting of grid refinement studies, Journal of Fluids Engineering 116 (3). doi:10.1115/1.2910291.
[33] J. W. Banks, T. Aslam, W. J. Rider, On sub-linear convergence for linearly degenerate waves in capturing schemes, Journal of Computational Physics 227 (14) (2008) 6985–7002. doi:10.1016/j.jcp.2008.04.002.
[34] C. J. Roy, Review of discretization error estimators in scientific computing, in: 48th AIAA Aerospace Sciences Meeting Including the New Horizons Forum and Aerospace Exposition, 2010.
[35] H. W. Liepmann, Elements of gas dynamics, New York : Wiley ; London : Chapman & Hall, 1957.
[36] F. G. Friedlander, The diffraction of sound pulses; diffraction by a semi-infinite plane, Proceedings of the Royal Society of London. Series A, Mathematical and physical sciences 186 (1006) (1946) 322–344.
[37] F. G. Friedlander, The diffraction of sound pulses; diffraction by an infinite wedge, Proceedings of the Royal Society of London. Series A, Mathematical and physical sciences 186 (1006) (1946) 344–351.
[38] L. Wakaba, S. Balachandar, On the added mass force at finite reynolds and acceleration numbers, Theoretical and Computational Fluid Dynamics 21 (2) (2007) 147–153. doi:10.1007/s00162-007-0042-5.
[39] P. Bagchi, S. Balachandar, Inertial and viscous forces on a rigid sphere in straining flows at moderate reynolds numbers, Journal of Fluid Mechanics 481 (2003) 105–148. doi:10.1017/S002211200300380X.
[40] J. N. Newman, Marine hydrodynamics, M.I.T. Press, Cambridge, MA ; London, 1977.
[41] R. D. Blevins, Applied fluid dynamics handbook, Van Nostrand Reinhold, New York, Wokingham, 1984.
[42] S. F. Hoerner, Fluid-dynamic drag : practical information on aerodynamic drag and hydrodynamic resistance, 3rd Edition, Hoerner Fluid Dynamics, Midland Park, N.J., 1965.
[43] H. L. Gauch, F. Montomoli, V. L. Tagarielli, On the role of fluid-structure interaction on structural loading by pressure waves in air, Journal of Applied Mechanics 85 (11). doi:10.1115/1.4040948.
[44] S. E. Rigby, A. Tyas, T. Bennett, S. D. Fay, S. D. Clarke, J. A. Warren, A numerical investigation of blast loading and clearing on small targets, International Journal of Protective Structures 5 (3) (2014) 253–274. doi:10.1260/2041-4196.5.3.253.